Research Square

Preprints are preliminary reports that have not undergone peer review.
They should not be considered conclusive, used to inform clinical practice,
or referenced by the media as validated information.

Study on the Effects of Surface Roughness on the Aerodynamic Characteristics of the CHN-T2 Wide-Body Aircraft Standard Model

Yang Tao

50323222@qq.com

China Aerodynamics Research and Development Center

Hexiang Wang

China Aerodynamics Research and Development Center

Junqiang Wu

China Aerodynamics Research and Development Center

Ce Zhang

China Aerodynamics Research and Development Center

Daxin Liao

China Aerodynamics Research and Development Center

Xin Peng

China Aerodynamics Research and Development Center

Neng Xiong

China Aerodynamics Research and Development Center

Jifei Wu

China Aerodynamics Research and Development Center

Weiyi Zeng

China Aerodynamics Research and Development Center

Hongbiao Wang

China Aerodynamics Research and Development Center

Dawei Liu

China Aerodynamics Research and Development Center

Article

Keywords: Surface Roughness, Wind Tunnel Testing, Wide-Range Reynolds Numbers, Wide-Body Aircraft Standard Model, Boundary Layer Characteristics

Posted Date: March 25th, 2026

DOI: https://doi.org/10.21203/rs.3.rs-9101726/v1

License: This work is licensed under a Creative Commons Attribution 4.0 International License.
Read Full License

Additional Declarations: There is **NO** Competing Interest.

Study on the Effects of Surface Roughness on the Aerodynamic Characteristics of the CHN-T2 Wide-Body Aircraft Standard Model

Hexiang Wang[1], junqiang Wu[2], Ce Zhang[1], Daxin Liao[1], Xin Peng[1], Neng Xiong[1], Jifei Wu[1], Hongbiao Wang[1], Weiyi Zeng[3], Yang Tao[1,*], Dawei Liu[1,*]

Affiliations

1 High-speed Aerodynamic Institute, China Aerodynamics Research and Development Center, Mianyang 62100, China

2 China Aerodynamics Research and Development Center, Mianyang 62100, China

3 Aerospace Technology Institute of CARDC, China Aerodynamics Research and Development Center, Mianyang 62100, China

Author contributions

H.W. was responsible for wind tunnel testing and manuscript writing. J.W. established the framework of the paper. C.Z. and D.L. carried out the CFD simulations, while X.P. handled the wind tunnel model preparation. N.X. and J.W. performed post-processing of the experimental data, and H.W. and W.Z. processed the CFD data. Y.T. and D.L. proposed the initial concept, supervised the project, and edited the manuscript.

Corresponding author

Correspondence to: Yang Tao[1,*], Dawei Liu[1,*]

Corresponding authors must provide their ORCID ID before resubmitting the final version of the manuscript. Non-corresponding authors are encouraged to link their ORCID.

Abstract

Under actual flight conditions, the surface of civil aircraft is subject to prolonged erosion from wind, frost, rain, snow, sand, dust, and insect debris. This cumulative surface degradation significantly alters the

skin microtopography, leading to progressive increases in surface roughness over flight time and consequently modifying the aircraft's aerodynamic characteristics. Similarly, in wind tunnel testing, particulate dust and organic impurities within the test section, accelerated by high-speed airflow, induce erosive wear and scratches on model surfaces. This progressive increase in surface roughness inevitably affects surface flow field characteristics, ultimately causing systematic deviations in aerodynamic performance evaluations. To address the impact of surface roughness on aerodynamic characteristics, this study combines wind tunnel experiments and numerical simulations to analyze the fundamental aerodynamic force characteristics of the wide-body aircraft standard model CHN-T2 under varying surface roughness levels. The research further investigates the influence of roughness on aerodynamic performance and transition characteristics at different angles of attack. Building on this, the study delves into the micromechanisms of surface roughness effects across a wide Reynolds number range. Results indicate that increased roughness elevates the total drag coefficient, advances the transition location from laminar to turbulent flow on wing surfaces, and enhances friction drag. The impact of roughness intensifies with increasing Reynolds number initially, subsequently stabilizing at higher values. Specifically, at low Reynolds numbers (3.3 million to 8 million), shock wave-induced transition dominates the outer wing region, with roughness increases causing forward movement of both shock wave and transition locations. At moderate Reynolds numbers (10 million to 15 million), roughness effects amplify: the laminar flow region diminishes on the inner wing, while TS (Tollmien-Schlichting)/CF (crossflow) instability-driven transition predominates in the outer wing, with roughness exacerbating laminar region reduction. When Reynolds numbers rise further (15 million to 45 million), roughness effects stabilize. The study also reveals roughness-induced alterations in boundary layer displacement thickness, momentum thickness, and velocity profiles. These findings provide critical guidance for improving wind tunnel test data reliability at high Reynolds numbers and optimizing aircraft surface treatment design.

Keywords: Surface Roughness, Wind Tunnel Testing, Wide-Range Reynolds Numbers, Wide-Body Aircraft Standard Model, Boundary Layer Characteristics

Introduction

Wind tunnel testing and Computational Fluid Dynamics (*CFD*) simulations play a pivotal role in the development of large transport aircraft. This synergy is primarily manifested in the fact that *CFD* provides critical guidance for the design of wind tunnel experiments, while experimental results, in turn, validate the reliability of numerical simulation methods, thereby informing further refinements to these numerical approaches[1]. In recent years, the aerospace community has consistently sought robust methodologies to enhance the fidelity of comparisons between *CFD* predictions and wind tunnel data; achieving this necessitates a precise understanding of the underlying mechanisms by which various factors influence such comparative analyses.

Among the myriad influencing factors, wing surface roughness, though seemingly minute, stands as a critical parameter that has long garnered significant attention from researchers. During wind tunnel testing, particulate dust within the tunnel or impurities entrained in the airflow, acting in concert with high-speed flows, can induce scratches and abrasive wear on the model surface, thereby altering its surface roughness. Similarly, in actual flight operations, the cumulative impact and erosion caused by wind, frost, rain, snow, sand, dust, and insect debris exert a substantial influence on surface roughness over time. The impetus for this study stems from an observed discrepancy in the lift and drag coefficients of the wide-body aircraft standard model CHN-T2. Specifically, slight deviations were noted between data obtained during the initial run in a continuous transonic wind tunnel and those recorded after 52 consecutive startup cycles, despite identical test conditions for both cases. This observation precipitated a focused investigation into the hypothesis that variations in the test model's surface roughness are responsible for the observed changes in aerodynamic force coefficients.

As early as the early 20th century, scientists initiated systematic investigations into surface roughness. A landmark contribution was made by Nikuradse in 1933, who introduced the concept of equivalent sand-grain roughness, a metric that remains fundamental to contemporary roughness research across various disciplines[2]. Building upon this foundation, Schlichting comprehensively synthesized the relationships between the geometric characteristics of diverse roughness element types and their equivalent sand-grain

roughness[3], thereby establishing a robust theoretical framework for subsequent studies. Currently, research on surface roughness permeates nearly every facet of the aerospace domain. Prominent applications include the study of wing icing phenomena[4–10], the assessment of fatigue life in turbomachinery components[11–16], and the development of passive flow control techniques leveraging engineered roughness elements[17–21].

Surface roughness has a significant impact on the aerodynamic performance of aircraft: On one hand, it alters the development of the boundary layer, thereby affecting the transition location, separation points, and the formation and bursting of laminar separation bubbles; on the other hand, it directly modifies surface friction stress and pressure distribution, thus influencing lift, drag, and moment characteristics. These effects not only determine aerodynamic efficiency and fuel economy but also directly affect flight controllability and safety. Particularly for modern civil aircraft, even a drag increase caused by surface roughness accounting for merely 1–2% of the total aircraft drag could result in hundreds of tons of additional fuel consumption over the entire service life, leading to substantial economic costs and environmental burdens.

Surface roughness significantly influences boundary layer transition. During the process of traveling wave instability excited by free-stream instabilities, small-amplitude roughness at appropriate surface locations may act as a catalyst. Alternatively, it can serve as a direct source of stationary vortex instabilities, such as Görtler vortices and stationary crossflow modes. Meelan et al.'s research demonstrated the pronounced effect of roughness on transition characteristics: polishing the leading edge of a swept wing reduced the root mean square roughness from 1.0 μm to 0.3 μm, shifting the transition location from 25–30% chord to 80% chord. Cebeci et al.[22] systematically investigated the impacts of environmental factors (e.g., rain, insect contamination, and ice accretion) on aerodynamic performance of aircraft wings. For rain effects, they found that heavy rainfall reduces the maximum lift coefficient by 30% and advances stall angle of attack. For insect contamination, impacts near the leading edge create localized roughness, altering boundary layer transition. Ice accretion introduces high surface roughness, leading to lift reduction, drag increase, and flow separation with separation bubbles that reduce the maximum lift coefficient by 20–30% and advance stall characteristics. Choudhari[23] studied the control of boundary layer transition over swept

wings using distributed roughness elements. By intentionally introducing small-scale roughness elements near the leading edge to excite subdominant crossflow modes, he found these modes alone cannot trigger transition but suppress the growth of dominant (most unstable) modes through nonlinear interactions, thereby delaying boundary layer transition and achieving laminar flow control. However, the roughness magnitude must be precisely optimized: insufficient roughness fails to suppress dominant modes, while excessive roughness prematurely induces transition. Ye et al.[24] investigated the effects of two typical roughness element geometries (randomly distributed sand grains and zigzag strips) with identical height and arrangement area on boundary layer transition and far-field noise in wind tunnel tests. Their study revealed that sand grains primarily generate low-speed disturbances in local regions, which evolve into streaks and eventually break down to form turbulent wedges. Zigzag elements trigger periodic shear layers, rapidly amplifying disturbances that fully transition to turbulence. Fan et al.[25] modified the γ-Reθ transition model by incorporating surface roughness effects. They defined roughness influence zones to locally adjust the transition model and track momentum thickness variations for modifying transition onset criteria. Additionally, they revised wall boundary conditions for specific turbulent dissipation rates to simulate roughness effects in fully turbulent regions. The improved model accurately predicts transition locations under varying roughness conditions in hypersonic flows. Ma et al. [26] conducted *CFD* simulations to analyze the impact of blade surface roughness on aerodynamic performance of transonic axial compressors under different altitudes (characterized by Reynolds number index, *RNI*). Results showed that increased roughness causes early transition, thicker boundary layers, forward shock movement, and premature flow separation, reducing efficiency, increasing losses, and lowering surge margin. Under high-altitude low-*RNI* conditions, although roughness effects weaken, the *RNI* itself significantly degrades compressor efficiency and stability.

Surface roughness significantly impacts aerodynamic performance, with numerous studies confirming its effects including lift reduction, drag surge, energy losses, and induction of complex flow separation and three-dimensional turbulent structures. Dwivedi[27] investigated the effects of introducing two types of roughness (E480 and E4220) at different chordwise positions (30% and 45%) on a NACA 4412 airfoil.

Results showed that appropriate roughness, while reducing lift, could effectively delay stall and lower drag. The E4220 roughness placed at 30% chord position demonstrated the best overall performance, offering new insights for passive flow control in high-angle-of-attack scenarios such as aircraft takeoff and landing. Chakroun et al.[28] studied the influence of varying roughness heights and locations on a NACA 0012 airfoil. Increased roughness was found to reduce lift and increase drag, with leading-edge roughness having the most detrimental effect on performance, whereas trailing-edge roughness had lesser impacts. Their research also revealed that roughness delays stall, thereby enhancing lift in post-stall regimes. U.S. Sandia National Laboratories[29] systematically investigated the effects of surface roughness (e.g., insect residue, paint peeling) on wind turbine blade aerodynamic performance and power generation under real-world conditions. Results indicated that increased roughness height and density led to reduced lift, elevated drag, and earlier boundary layer transition, with maximum lift-to-drag ratios declining by up to 40.8% and corresponding annual energy production losses reaching 2.3%. Lim et al.[30] explored the impact of additive manufacturing-induced surface roughness on compressor blade aerodynamics by defining three roughness levels. They observed nonlinear increases in total pressure loss with roughness growth, with performance degradation intensifying when $k^+_s > 20$. Kumar et al.[31] conducted large eddy simulations (LES) to study leading-edge roughness effects on flow separation over a NACA 4412 airfoil. Their findings revealed that roughness structures induce "flow channeling", creating alternating high and low speed regions, and excite various hairpin vortex structures. These phenomena enhance flow three-dimensionality and turbulence activity, causing significant spanwise variation in trailing-edge separation locations, earlier separation onset, and highly non-uniform separation patterns.

Overall, existing research has primarily focused on components with relatively low Reynolds numbers, such as compressors. The mechanisms by which surface roughness influences boundary layer separation and transition under high Reynolds number conditions remain unclear. When conducting wind tunnel tests across a wide range of Reynolds numbers, it is necessary to deeply analyze the impact of roughness on the boundary layer characteristics and aerodynamic performance of model surfaces under different Reynolds number conditions. Therefore, the primary objective of this study is to explore the governing laws of how

surface roughness affects the aerodynamic and transition characteristics of transonic transport aircraft under high Reynolds number conditions, and to analyze the underlying mechanisms. This paper is organized as follows: First, the CHN-T2 geometric model, numerical methods, wall treatment, and roughness correction methods are introduced. Subsequently, by combining wind tunnel test data with Computational Fluid Dynamics calculations, the influence of roughness on aerodynamic characteristics is analyzed, with a focus on revealing the intrinsic mechanisms by which increased roughness alters pressure distribution and skin friction drag distribution. Finally, the quantitative relationships between roughness and boundary layer parameters (including total thickness, displacement thickness, momentum thickness, and shape factor) under a wide range of Reynolds numbers are systematically elaborated. This work provides a theoretical basis for improving the reliability of wind tunnel test data at high Reynolds numbers and for the design of aircraft surface treatments.

Methods

CHN-T2 Geometry and Mesh Generation Strategy

The object of this study is the wide-body aircraft standard model CHN-T2 (as shown in Fig. 1), designed by the China Aerodynamics Research and Development Center. The model features a twin-aisle fuselage with a length of 63.068 meters and a wingspan of 61 meters. Its cruise Mach number is 0.85, with a cruise altitude ranging from 10 to 12 kilometers. The aircraft employs a supercritical wing, which exhibits typical flow field characteristics such as shock-induced separation and transition. Detailed geometric and aerodynamic parameters are listed in Table 1.

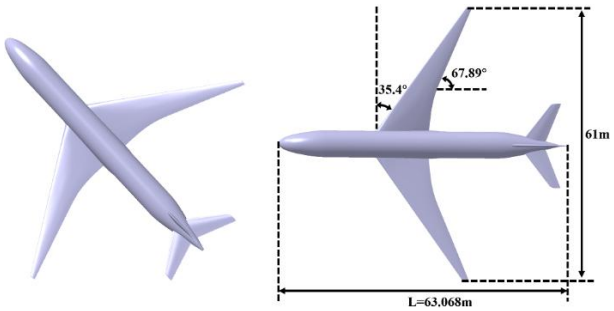


Fig. 1 Schematic geometry of the CHN-T2 model.

Numerical Method

(a) Governing Equations and Transition Models

The general form of the three-dimensional Navier-Stokes (N-S) equations is as follows:

$$\frac{\partial Q}{\partial t}+\frac{\partial}{\partial z}(F_1+G_1)+\frac{\partial}{\partial y}(F_2+G_2)+\frac{\partial}{\partial z}(F_3+G_3)=\dot{S} \tag{1}$$

Where Q is the vector of dependent variables; F_1, F_2, and F_3 are the inviscid flux vectors;G_1, G_2, and G_3 are the viscous flux vectors; and S is the source term vector.

To accurately simulate phenomena such as boundary layer separation and transition over the CHN-T2 surface, the Shear Stress Transport (*SST*) turbulence model coupled with a transition model is employed. This is a four-equation transition model based on the turbulence equations, incorporating two additional transport equations. Proposed by Menter and further refined by Langtry et al., this model comprises two transport equations: one for the intermittency factor and another for the transition criterion based on the momentum thickness Reynolds number. For a more detailed description of the equations, please refer to Ref [32].

(b) Wall Treatment and Roughness Correction

A full y^+ wall treatment approach is employed. This is an adaptive, all-range applicable wall treatment method that utilizes a hybrid wall function, providing effective boundary conditions for fluid, energy, and turbulent quantities across a wide range of near-wall grid densities. To simulate the influence of roughness on the turbulent boundary layer, we refer to Knopp's roughness correction method. This method does not require modification of the *SST* model itself; instead, it applies specific wall functions to velocity, temperature, turbulent dissipation rate, and specific dissipation rate. This characteristic allows it to be effectively integrated into the *SST* four-equation transition model. The study found that it significantly improves the prediction of TS-wave-induced transition over rough airfoil surfaces[33] .

Specifically, the corrected dimensionless wall velocity V^+ can be expressed as:

$$V^+ = \frac{1}{\kappa}\log\left(\frac{d_e}{d_0}\right) = \frac{1}{\kappa}\log\left(\frac{d^+ + d_0^+}{d_0^+}\right) \tag{2}$$

$$d_0^+ = \begin{cases} 0.56\left(R^+ / R_{\text{smooth}}^+\right)^{2.5} & ;R^+ < R_{\text{smooth}}^+ \\ 0.63\zeta(R^+) + 0.028R^+ & ;R_{\text{smooth}}^+ \le R^+ \le R_{\text{rough}}^+ \\ 0.031R^+ - 0.27 & ;R^+ > R_{\text{rough}}^+ \end{cases} \tag{3}$$

Where κ is the von Karman constant, d_0 is the displacement origin of the boundary layer, d_e is the effective displacement origin of the boundary layer, d^+ is the dimensionless wall distance, and d_0^+ denotes the point where the viscous sublayer satisfies the logarithmic layer solution. R^+ is the roughness function, expressed as $R^+ = \frac{r\rho u_*}{\mu}$, where r is the equivalent sand-grain roughness height, ρ is the density, u^* is the velocity scale, μ is the dynamic viscosity. R^+_{smooth} and R^+_{rough} represent the roughness functions corresponding to fully smooth and fully rough surfaces, respectively.

The corrected dimensionless temperature T^+ based on the hybrid wall function is expressed as:

$$T^+ = e^{\left(-S'\right)}Prd^+ + e^{\left(-\frac{1}{S'}\right)}Pr_t\left[\frac{1}{k}\ln\left(\frac{d^+ + d_0^+}{d_0^+}\right) + U\right] \tag{4}$$

Where Pr is the Prandtl number, S is the blending function, and U is the velocity at the intersection of the logarithmic layer and the viscous sublayer governing the thermal distribution. The corrected turbulent dissipation rate can be expressed as:

$$\varepsilon^{+} = \gamma \frac{2k^{+}}{\left(d^{+}\right)^{2}} Y + (1-\gamma)\frac{1}{\kappa d^{+}} \tag{5}$$

Where k^{+} is the dimensionless turbulent kinetic energy, and γ is a function of the wall-distance Reynolds number.

The corrected specific dissipation rate is expressed as:

$$\omega^{+} = \gamma S_{\mathrm{r}} + (1-\gamma)\frac{1}{\kappa\sqrt{C_{u}}} \tag{6}$$

Where S_{r} is a polynomial defined by R^{+}, and C_{u} is $\mathrm{k}-\omega$ model coefficient.

The CHN-T2 configuration features a leading-edge sweep angle of up to 35.4°, which leads to an increased spanwise flow velocity component and a significant enhancement of crossflow effects. Existing research results [34,35] indicate that in low free-stream turbulence environments, the stationary crossflow mode is the dominant crossflow instability mechanism in the boundary layer of swept wings, and surface roughness has a significant impact on stationary crossflow transition. Based on this, Menter introduced a crossflow correction to the $\gamma - Re_{\theta}$ model [36]. The corrected model incorporates a roughness parameter. Specifically, the transport equation for the transition momentum thickness Reynolds number is modified as follows:

$$\frac{\partial(\rho \mathrm{Re}_{\theta})}{\partial t} + \nabla\cdot(\rho U \mathrm{Re}_{\theta}) = P_{\theta} + D_{\mathrm{SCF}} + \nabla\cdot\left(\sigma(\mu+\mu_{t})\nabla \mathrm{Re}_{\theta}\right) \tag{7}$$

Where D_{SCF} is the crossflow correction term, whose expression depends on the stationary crossflow correlation Re_{SCF}. The crossflow sink term D_{SCF}, is not active globally; instead, its activation is controlled by comparing Re_{SCF} with the transition momentum thickness Reynolds number $Re_{\theta \mathrm{t}}$. When significant

crossflow instability exists in the flow, Re_{SCF} decreases. Once $Re_{SCF} < Re_{\theta}$, the term D_{SCF} is triggered, thereby accelerating the transition process.

(c) Wind Tunnel and Test Models

The full-model force measurement test was conducted in a transonic wind tunnel. Fig. 2 shows the physical view of the CHN-T2 wind tunnel test model, which is a 1:39.1 scaled model. A sting-mounted six-component strain balance was employed to measure the aerodynamic forces acting on the model.



Fig. 2 CHN-T2 wind tunnel test model

(d) Roughness parameter settings

In wind tunnel tests, the Reynolds number per unit length is higher than that of actual flight (approximately the inverse of the model scale). To ensure aerodynamic similarity with full-scale flight, the model surface roughness must be scaled down accordingly; otherwise, the relative roughness of the model would be excessively high, introducing additional drag errors. NASA conducted extensive tests in the NTF wind tunnel and ultimately established a standard for the centerline averaged roughness (*Ra*) of approximately 0.3 μm[37] . The test wind tunnel in this study has a test section size and Reynolds number range similar to those of the NTF. After actual measurements at various locations across the entire model using a profilometer (with meticulous polishing applied to the entire surface), the analysis and evaluation indicated an arithmetic mean roughness of approximately 0.1 μm prior to the first wind tunnel startup. In the final

test phase (after 52 startups), however, the combined action of contaminants in the wind tunnel and high-speed airflow caused certain scratches and wear on the model surface. Subsequent measurements yielded an arithmetic mean roughness value of approximately 1 μm. Fig. 3 shows photographs of the model surface condition at the end of the first test phase and during the final test phase. Regarding the calculation of equivalent sand-grain roughness, this paper employs the correlation proposed by Koch and Smith[38] , whereby the equivalent sand-grain roughness is derived from the arithmetic mean roughness Ra.

$$k_s = 6.2R_a \tag{8}$$

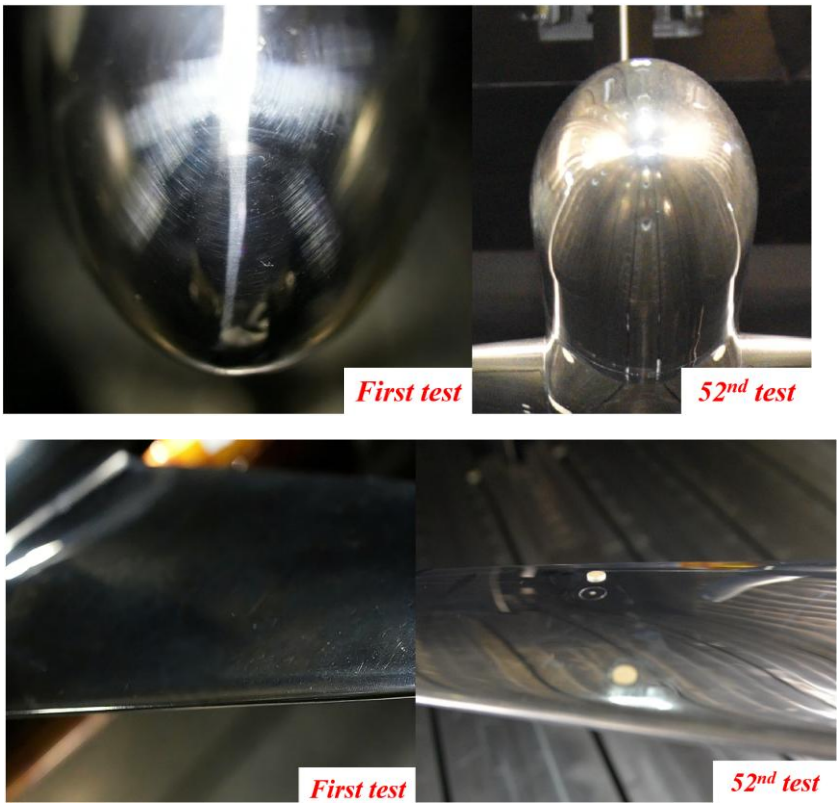


Fig. 3 Surface views of the CHN-T2 model after the first and 52nd startups

(e) Grid and Boundary Conditions

Multi-block hexahedral compatible computational grids were generated. The CHN-T2 standard model was partitioned into topological blocks. The grid topology and boundary conditions are illustrated in Fig. 4. The far-field boundary is subjected to free-stream conditions, while the lateral sides of the model are designated

as symmetry planes. The fluid domain adopts a rectangular prism shape. The upstream boundary is positioned 30L ahead of the model, and the downstream boundary is located 50L behind it. With a domain width of 15L, both the top and bottom boundaries of the computational domain are set 15L away from the model surface.

Coarse, medium, and fine structured grids were employed for the grid independence study. To ensure accurate resolution of the boundary layer flow, The y^+ values for all three mesh groups are approximately 1. The grid independence verification was conducted at a Mach number of 0.85, a Reynolds number based on the mean aerodynamic chord of 4.5×10^7, and an angle of attack (AoA) of 2°. The computational results are presented in Table 2. The results indicate that as the grid resolution increases, both the lift and drag coefficients exhibit a decreasing trend. When further refined to the fine grid, the aerodynamic forces and moment coefficients tend to stabilize. Consequently, a medium grid density (13 million cells) was selected to satisfy the requirements for subsequent numerical simulations.

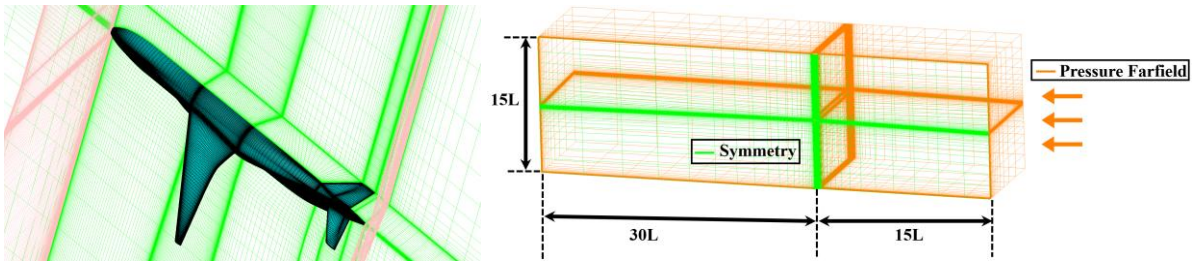


Fig. 4 Schematic of grid topology and boundary conditions

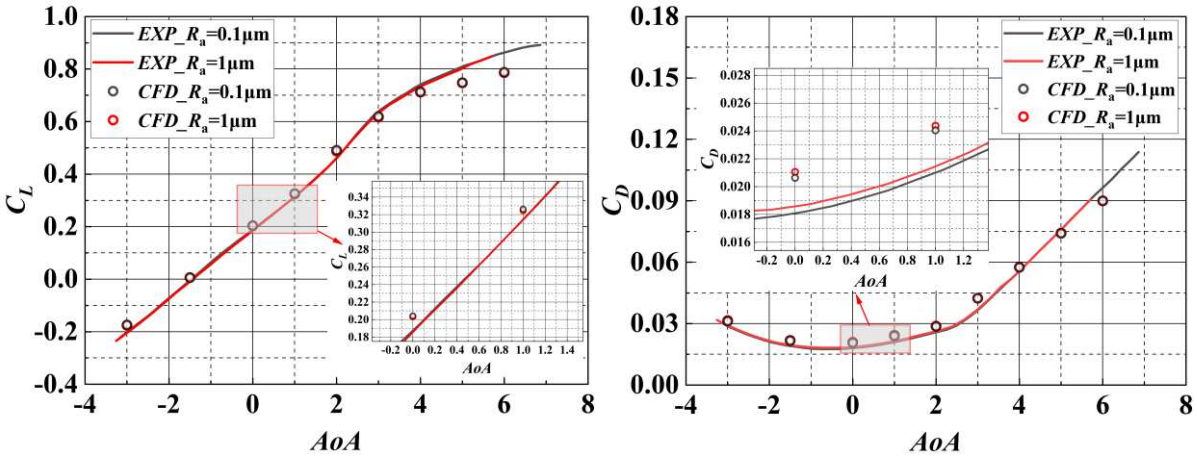
Results

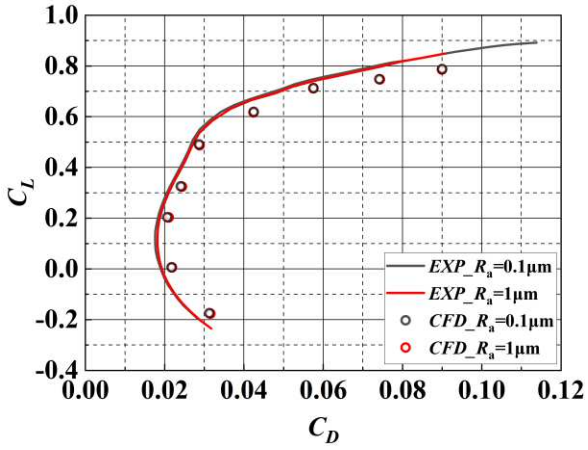
Study on the Effect of Roughness on the Basic Aerodynamic Characteristics of CHN-T2

Fig. 5 compares the numerical simulations and experimental results for the roughness cases of Ra=0.1μm and Ra=1μm. The comparison condition is: Ma=0.85, with stagnation pressure and temperature being

P_0=115000 Pa and T_0=301K, respectively, at a reference Reynolds number of 3.3 million. It can be observed from the figure that the lift coefficient exhibits an approximately linear increase within the *AoA* range of -3° to 2°. As the *AoA* continues to increase, flow separation occurs on the upper surface, causing the lift to deviate from linear growth. Compared to the *Ra*=1μm case, the *Ra*=0.1μm case demonstrates a lift coefficient increase of approximately 0.002. Significant discrepancies between the calculated and experimental values are observed at high angles of attack. This is likely because the RANS method struggles to accurately capture flow separation details under such conditions, resulting in an underestimation of the lift coefficient. However, the overall trends between the two are consistent. From the drag curves, it is evident that drag initially decreases and then increases with rising *AoA*. This phenomenon may be attributed to pronounced flow separation on the wing's lower surface at large negative *AoA*, forming a trailing-edge separation bubble that increases base pressure and consequently leads to higher pressure drag. As the *AoA* approaches 0°, the flow gradually reattaches, reducing the separated region and thus lowering the pressure drag. With a further increase in *AoA*, flow separation gradually appears on the upper surface, and the separated region expands, causing a significant rise in pressure drag, which is reflected in the increased slope at positive *AoA*. Fig. 6 illustrates the drag components, showing that pressure drag dominates the non-linear variation trend of the total drag coefficient within this *AoA* range; hence, the variation in pressure drag determines the total drag change. The *Ra*=0.1μm case results in a drag coefficient reduction of approximately 0.0025 compared to the Ra=1μm case, and the drag difference between *CFD* and *EXP* is consistent for both roughness levels. Fig. 6 presents the variation of drag components with *AoA*. The change in pressure drag aligns with the trend of total drag. The influence of roughness on skin friction drag is more pronounced. Specifically, friction drag increases with *AoA* from -3° to 1°, but decreases as *AoA* rises from 1° to 6°. The variation in friction drag coefficient between the two roughness levels closely matches the total drag coefficient variation, indicating that at a Reynolds number of 3.3 million, roughness primarily affects the magnitude of skin friction drag as the angle of attack increases.

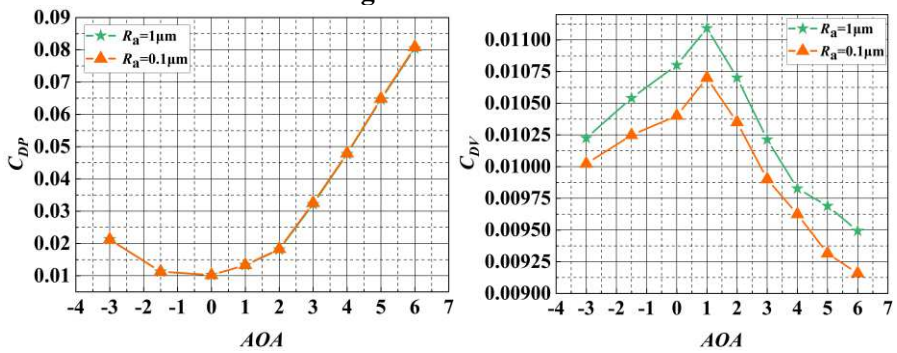
Fig. 7 presents the skin friction coefficient contours for the two roughness cases at angles of attack of 2° and 6°. To visually demonstrate the variation in skin friction due to roughness, The skin friction drag on the upper surface was extracted at the cross-sections $\eta = 0.05$ and $\eta = 0.45$. It can be observed that at 2° angle of attack, with the increase in roughness, the transition location on the cross-section moves significantly upstream. This is likely attributed to the enhancement of crossflow disturbances induced by the higher surface roughness. On the cross-section, the transition location shifts slightly upstream, which may be caused by the upstream movement of the shock wave under higher roughness, thereby triggering earlier transition. At a 6° angle of attack, Fig. 7(b) shows the surface streamlines, indicating that massive flow separation has occurred over the outboard wing section. Examining the cross-section, it is evident that compared to the 2° case, the disturbances caused by crossflow are weakened, resulting in transition locations that are relatively close to each other under the two roughness conditions. On the cross-section, the influence of flow separation disrupts the stable development of the boundary layer, eliminating the distinct transition process; hence, the curves appear relatively flat. The figure also illustrates the spatial flow fields at this cross-section for both roughness levels. With increased roughness, the separation point moves upstream, the separated region over the airfoil expands slightly, and the separation zone formed at the trailing edge intensifies.





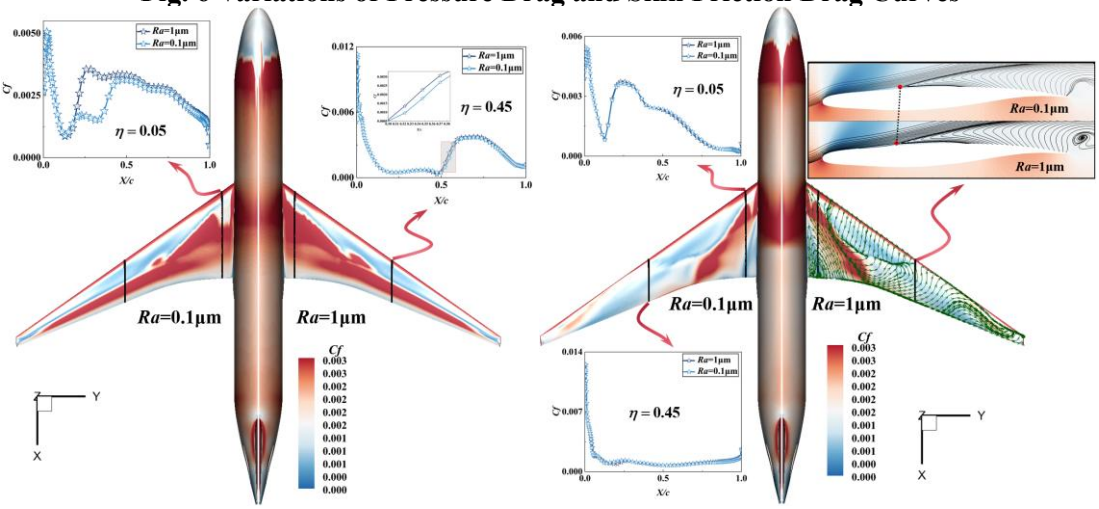
322

323 **Fig. 5 Comparison of Aerodynamic Coefficients between EXP and CFD under Different**
324 **Roughness Conditions**



325

326 **Fig. 6 Variations of Pressure Drag and Skin Friction Drag Curves**



327

328 (a) (b)

329 **Fig. 7 Comparison of skin friction coefficient contours for the two roughness cases at different**
330 **angles of attack: (a) 2°, (b) 6°**

Study on the Mechanism of Micron-Scale Roughness Effects over a Wide Range of Reynolds Numbers

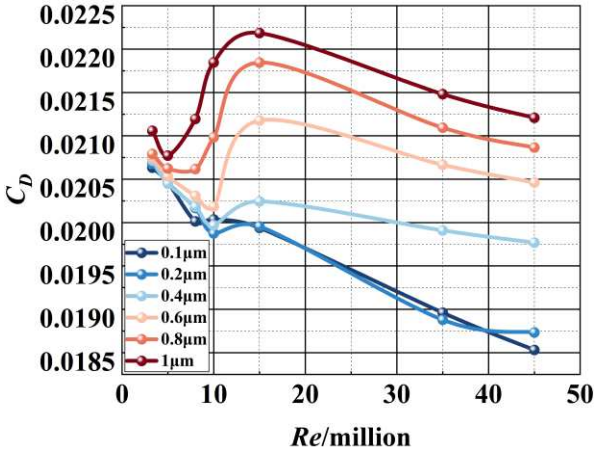
In wind tunnel environments, minute particles impact the wing surface at specific velocities during testing. This phenomenon suggests that the surface roughness may remain dynamic throughout the test duration. Consequently, the two roughness cases examined in the previous section are further refined. This study focuses on the effects of roughness, ranging from 0.1μm to 1μm, on aerodynamic characteristics, boundary layer behavior, and transition features across the entire experimental Reynolds number range (based on mean aerodynamic chord, from 3.3 million to 45 million). The geometric model remains the CHN-T2 scaled model (scale factor: 1:39.1). The aerodynamic conditions are listed in

Table **3**.

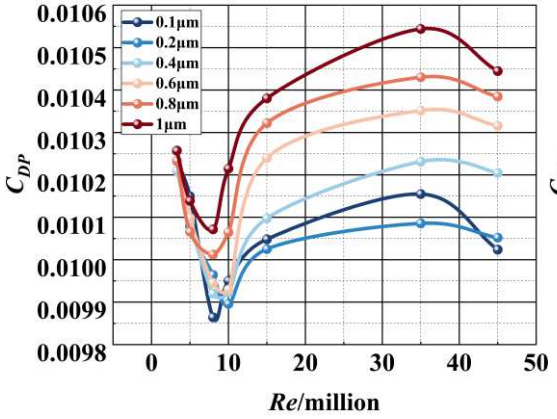
(a) Aerodynamic Characteristics

Fig. 8 presents the variation curves of drag and its components under different Reynolds numbers for roughness levels ranging from 0.1μm to 1μm under the specified aerodynamic conditions. It can be observed that, when surface roughness is considered, the total drag, pressure drag, and skin friction drag all increase with rising roughness. At a Reynolds number of 3.3 million, the total drag increment induced by roughness is 0.00043, corresponding to an increase of approximately 2.08%. When the Reynolds number increases to 15 million, the total drag increment rises to 0.00225 (about 11.28%), and further increases to 0.00268 (about 13.46%) at a Reynolds number of 45 million. It is evident that at lower Reynolds numbers, the drag variation with roughness is relatively small. As the Reynolds number increases to 15 million, the sensitivity of drag to roughness increases. With further Reynolds number increments, the total drag increase with roughness tends to stabilize. The variations of pressure drag and skin friction drag with respect to roughness are almost consistent with the trend of total drag. The above analysis fully demonstrates that

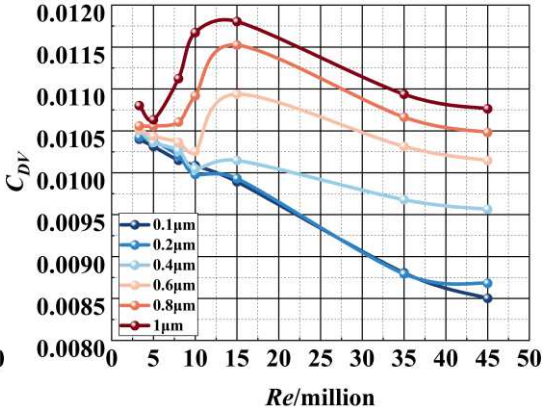
roughness has a significant impact on the drag characteristics of the CHN-T2, particularly at high Reynolds numbers. To investigate the underlying internal mechanisms, subsequent analyses will be conducted in-depth regarding pressure distribution, transition characteristics, and boundary layer behavior.



(a) Total drag



(b) Pressure Drag



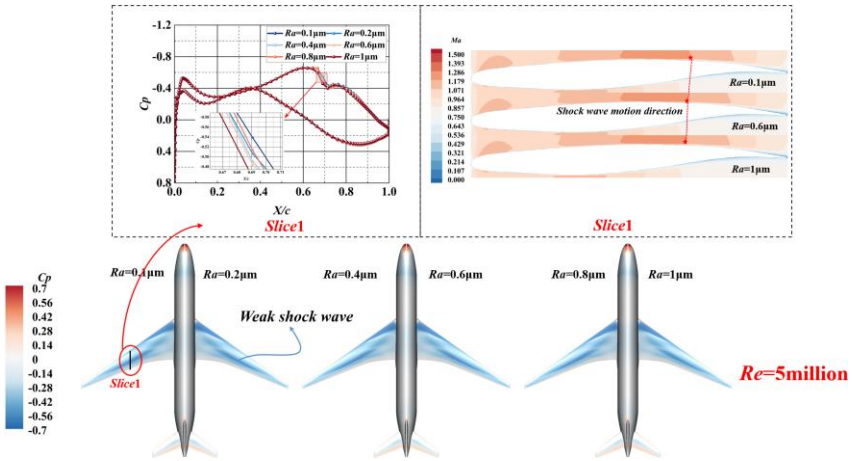
(c) Skin friction drag

Fig. 8 Variation curves of drag and its components at different roughness levels

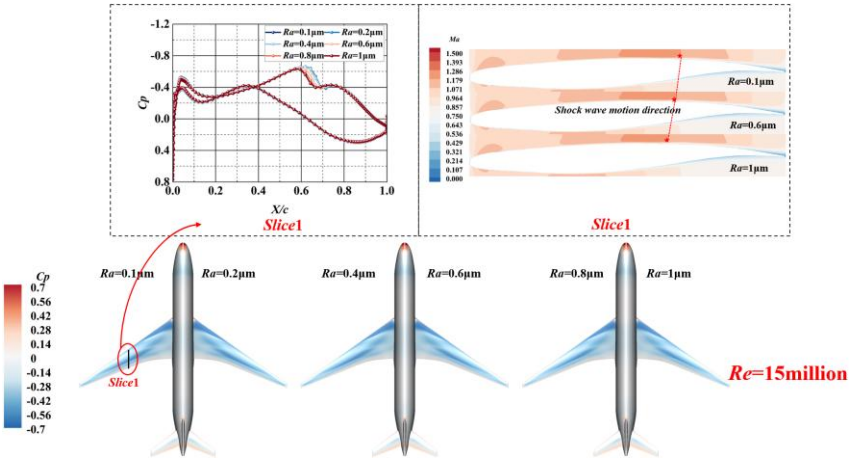
(b) Pressure Distribution Characteristics

Fig. 9 illustrates the wing surface pressure contours and the variation of shock wave position at cross-section Slice 1 under three Reynolds numbers: *Re* = 5 million, *Re* = 15 million, and *Re* = 45 million. At *Re* = 5 million, the pressure distribution curve at Slice 1 (Fig. 9a) indicates that differences among various roughness levels are primarily manifested in the pressure distribution near the shock wave. As roughness

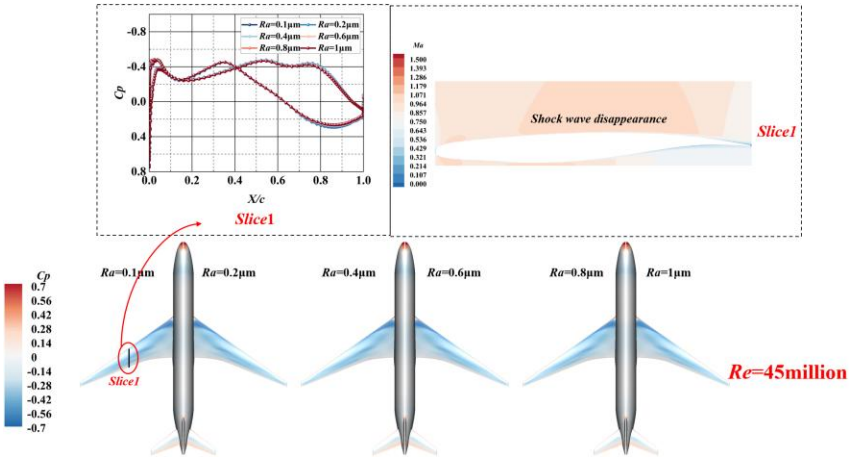
increases, the shock wave position gradually moves upstream. Due to the small angle of attack and weak shock wave intensity, combined with the micron-scale roughness variation, the displacement is relatively small (approximately 1.5% of the local chord length when *Ra* increases from 0.1μm to 1μm).When the Reynolds number increases to 15 million, the pressure contours on the upper surface of the CHN-T2 show that the negative pressure region in the shock wave area decreases with increasing roughness, indicating a gradual weakening of shock wave intensity. This is also evident from the pressure distribution curve at Slice 1, where the peak pressure at the location of the pressure surge decreases significantly compared to lower roughness levels. Nevertheless, compared to the condition at *Re* = 5 million, the upstream movement of the shock wave caused by increased roughness is more pronounced (approximately 5% of the local chord length when *Ra* increases from 0.1μm to 1μm). It can be observed from the figures that the high-pressure region at the shock wave position diminishes (reducing the pressure difference across the shock), thereby contributing to an increase in pressure drag. When the Reynolds number further increases to 45 million, the pressure contours of the CHN-T2 at various roughness levels exhibit a smaller overall surface negative pressure region compared to the *Re* = 15 million case, a characteristic also reflected in the pressure curves. Notably, the shock wave at the Slice 1 cross-section disappears. This phenomenon may be attributed to boundary layer thickness variations altering the effective aerodynamic shape and flow structure. Specifically, the increase in Reynolds number weakens viscous effects and thins the boundary layer. This effectively modifies the airfoil's geometry, increasing the effective camber and local curvature, thereby altering the pressure distribution pattern to the extent that the shock wave vanishes.



(a) *Re*=5million



(b) *Re*=15million



(c) *Re*=45million

Fig. 9 *Re*=5million, 1500million, 4500million Pressure contours and pressure distribution characteristics at the cross-section

(c) Transition characteristics

Fig. 10 presents the skin friction drag contours of the CHN-T2 and the skin friction distribution curves at cross-section Slice 2 under various roughness levels across a wide Reynolds number range. At a Reynolds number of 3.3 million, when Ra = 0.1μm, the laminar flow region near the fuselage nose is extensive. However, as roughness increases to 1μm, the laminar region rapidly diminishes. This phenomenon may be attributed to the low Reynolds number regime, where the initial amplitude of crossflow instability is low, requiring disturbances to propagate over a longer distance to accumulate sufficient energy to reach the transition threshold. This explains why a relatively long laminar region is maintained at the fuselage nose when the roughness is 0.1μm. As roughness increases to 1μm, the critical momentum thickness Reynolds number at the nose is significantly modified by the roughness correction term, effectively altering the transition criterion and causing the laminar region to shrink rapidly. In contrast, the variation of the laminar region over the wing with increasing roughness is less pronounced. At a Reynolds number of 5 million, the laminar region at the nose remains largely unchanged with increasing roughness. This is because the elevated Reynolds number causes the critical momentum thickness Reynolds number to quickly reach the threshold, submerging the relative contribution of the roughness correction term. However, the influence of roughness over the wing becomes significantly more pronounced compared to the 3.3 million case. It is observed that with increasing roughness, the influence range of the crossflow effect at the wing root expands from 0.027b to 0.034b. This expansion occurs because increased roughness enhances the crossflow intensity ($H_{\text{crossflow}}$) at the wing root. The crossflow effect acts first at the wing root due to the larger local chord length and consequently higher local Reynolds number, which reaches the transition threshold earlier. The intensified crossflow lowers the critical momentum thickness Reynolds number, causing the laminar region at the wing root to shift spanwise. The figure also displays the skin friction coefficient curves at the outer wing section (Slice 2) for Re =5 million. As roughness increases, the transition location moves gradually upstream, and the affected region coincides with the shock wave interaction region discussed in the previous section. Therefore, it can be inferred that the transition in this area is induced by shock wave

interference. As the Reynolds number increases to 8 million, the increase in roughness further exacerbates the crossflow effect at the wing root, with the influence range expanding from 0.058b to 0.157b as Ra increases from 0.1μm to 1μm, and the effect on the outer wing becomes more evident. The variation in skin friction at the Slice 2 cross-section of the outer wing is similarly caused by the shock wave. When the Reynolds number reaches 15 million, the influence of roughness at the wing root continues to expand. Furthermore, at *Ra* = 1μm, the laminar region over the outer wing drastically reduces compared to the *Ra* = 0.1μm case. This can be explained by the fact that under high Reynolds numbers, the disturbance energy of crossflow instability is strong. In this scenario, roughness acts as a "catalyst" for crossflow disturbances. The roughness elements generate local disturbances within the laminar boundary layer, and when the disturbance energy exceeds the stability threshold of the laminar flow, transition occurs prematurely. The variation in skin friction coefficient shown at the Slice 2 cross-section validates the above hypothesis. Under this Reynolds number, crossflow instability intensifies dramatically, triggering transition at approximately 10% chord length from the leading edge. Moreover, as roughness increases, this transition occurs correspondingly earlier.

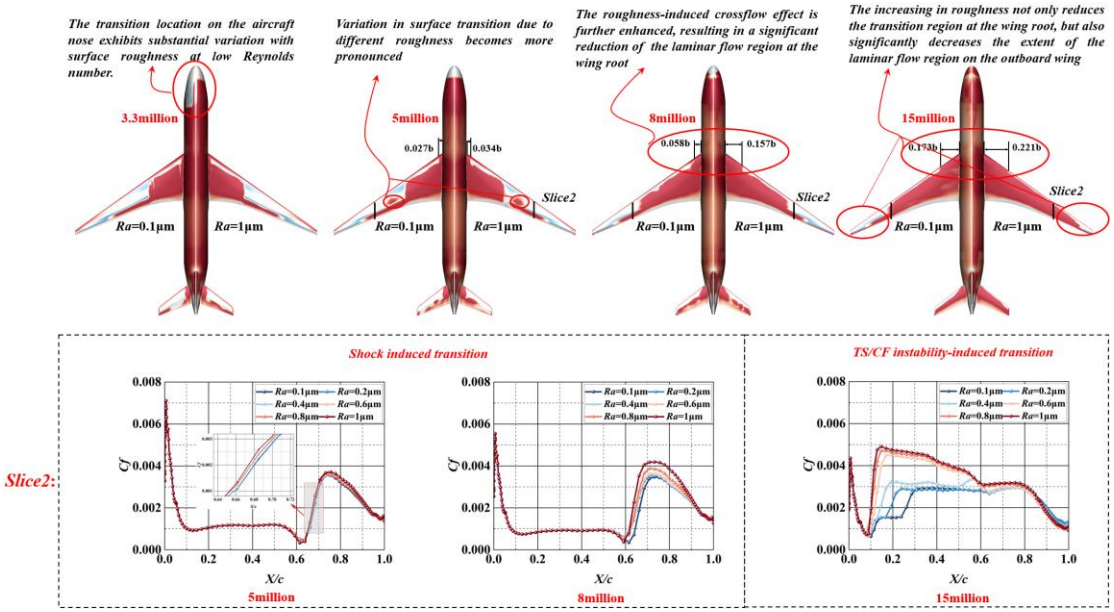


Fig. 10 Friction Resistance Contours under Various Roughness Conditions over a Wide Reynolds Number Range for CHN-T2, and the Friction Resistance Variation at Slice 2

(d) Boundary Layer Characteristics

To gain deeper insights into the mechanism of roughness effects over a wide Reynolds number range, the surface boundary layer on the Slice 2 cross-section was extracted. The airfoil geometry of the section and the boundary layer probe distribution are illustrated in Fig. 11. Fig. 12 presents the boundary layer characteristics at the Slice 2 section under Re=5 million. Fig. 12(a) depicts the variation of boundary layer thickness. As mentioned previously, the transition in this case is induced by a shock wave. Prior to transition, the boundary layer is laminar, and variations in roughness have negligible effects on it. However, within the transition region, the boundary layer thickness increases slightly with increasing roughness. Once the flow becomes fully turbulent, the boundary layer thickness converges again despite roughness variations. Fig. 12(b) shows the displacement thickness δ^*, which reflects the strength of the "displacement effect" of the airfoil in the streamwise direction. Local peaks indicate stronger displacement effects and more significant influences on the flow field. As observed in the figure, small peaks occur at the leading edge and at the mid-chord shock position. The peak at the leading edge may be attributed to the rapid velocity change from 0 to *Ue* near the stagnation point, creating a steep velocity gradient. This steep velocity profile causes a rapid accumulation of δ^* over a small range, resulting in a local peak at the leading edge. As the flow develops, shock-induced transition occurs, and the displacement effect strengthens again. Fig. 12(c) presents the shape factor distribution(H_{12}), which serves as an auxiliary indicator for identifying transition locations. Within the laminar boundary layer, H_{12} ranges between 2.5 and 3.3. Upon transition, H_{12} drops sharply. After the flow becomes fully turbulent, H_{12} stabilizes around 2. Under this Reynolds number, the influence of roughness is primarily manifested in the transition region. Fig. 12(d) illustrates the momentum thickness distribution. The momentum thickness increases dramatically when the flow enters the transition and fully turbulent regions, and it also exhibits a slight increase with increasing roughness.

Fig. 13 presents the boundary layer characteristic curves at the Slice 2 section under *Re*=10 million. As observed in Fig. 13(a), the influence of roughness on boundary layer thickness is significantly amplified at

461 this Reynolds number. For *Ra*=0.1, 0.2, and 0.4 μm, transition remains shock-dominated; however, the
462 divergence in thickness variation becomes more pronounced compared to the *Re*=5 million case, and the
463 final boundary layer thickness at the trailing edge increases with roughness. When *Ra*=0.6, 0.8, and 1 μm,
464 transition occurs upstream of the shock wave (the transition locations for these three roughness levels are
465 schematically indicated by arrows of three colors in the figure). Furthermore, as roughness increases, the
466 transition region shifts progressively upstream, resulting in a more substantial increase in boundary layer
467 thickness. Specifically, the total boundary layer thickness at the trailing edge for Ra=1 μm increases by
468 approximately 0.8 mm (80%) compared to *Ra*=0.1 μm. Examining Figures 13(b) and 13(d), the impact of
469 roughness on displacement thickness and momentum thickness is enhanced relative to the *Re*=5 million
470 scenario. At *Ra*=1 μm, the variations in both displacement and momentum thickness are more significant
471 compared to other roughness levels. Observing the streamwise evolution, during the initial flow
472 development (when the boundary layer is laminar), the variations of both parameters remain nearly identical
473 across different roughness levels. As the flow develops, the *Ra*=1 μm case undergoes transition first.
474 Following the completion of transition, the slopes of both thickness parameters increase for the *Ra*=1 μm
475 case. Similarly, for the remaining roughness levels, the slopes of momentum thickness and displacement
476 thickness also increase upon exiting their respective transition regions.

477 Fig. 14 presents the boundary layer characteristic curves at the Slice 2 section under *Re*=15 million. At this
478 condition, the transition region is concentrated between 8% and 15% chord. Since the boundary layer
479 development trends for the various roughness levels are nearly identical, observing Figure 14(a) reveals
480 that the thicknesses are almost consistent across different roughness levels in the laminar region. The
481 thickness discrepancies induced by roughness begin to form within the transition region. After entering the
482 fully turbulent region, the boundary layer thickness differences caused by roughness are fully manifested
483 and persist until the trailing edge. Specifically, the boundary layer thickness for the 1 μm roughness
484 increases by approximately 0.5 mm compared to the 0.1 μm case. This increment is smaller than that
485 observed at *Re*=10 million. The reason is that at *Re*=10 million, the 0.1 μm case maintained a laminar

boundary layer over 60% of the chord length, resulting in slower growth. In contrast, at *Re*=15 million, the 0.1 μm case undergoes transition immediately at the leading edge and remains turbulent throughout the rest of the chord, thereby reducing the relative increment. Observations of Fig. 14(b) and 14(d) indicate that the variations in displacement thickness and momentum thickness stratify at the 0.6 μm threshold. This suggests that under *Re*=15 million, roughness values greater than or equal to 0.6 μm exert an increased influence on the boundary layer flow.

Fig. 15 presents the boundary layer characteristic curves at the Slice 2 section under *Re*=45 million. At this condition, the airfoil surface is entirely within the fully turbulent regime. As observed in Fig. 15(a), 15(b), and 15(d), stratification in boundary layer thickness, displacement thickness, and momentum thickness occurs even at a roughness of 0.4 μm, indicating that higher Reynolds numbers impose stricter requirements on surface roughness. Fig. 15(c) illustrates the variation of the shape factor in the turbulent boundary layer, showing that the overall H_{12} distribution remains below 2.2.

The preceding sections have described the variations in boundary layer characteristic curves for different roughness levels across various Reynolds numbers. This section will focus on the boundary layer thickness, analyzing the trend in boundary layer thickness under the coupled effects of roughness and Reynolds number. As is well known, boundary layer thickness decreases with increasing Reynolds number. In Fig. 12(a), the boundary layer thickness (referring to the final thickness at the trailing edge) for all roughness levels at *Re*=5 million is approximately 1.45 mm. When the Reynolds number increases to 10 million, the thickness for *Ra*=0.1 μm decreases to 1.15 mm, which aligns with the aforementioned general principle. However, when roughness increases to 0.6 μm or higher, the thickness rises to over 1.7 mm. This is attributed to the earlier onset of transition, which allows the turbulent boundary layer to develop sooner. Since turbulent boundary layers grow faster than laminar ones, the final thickness exceeds that observed at *Re*=5 million. As the Reynolds number further increases to 15 million, the transition location moves even further upstream. For all roughness levels, transition occurs near the leading edge. Consequently, even at

the lowest roughness (*Ra*=0.1 μm), the total boundary layer thickness exceeds 1.45 mm (the value at *Re*=5 million). When the Reynolds number reaches 45 million, although the turbulent region is longer than that at 15 million, the total boundary layer thickness actually decreases. For instance, compared to the *Re*=15 million case, the total thickness at *Re*=45 million and *Ra*=0.1 μm is reduced by 0.17 mm. A similar pattern is observed for other roughness levels. This indicates that the introduction of surface roughness complicates the behavior of boundary layer characteristics across a wide Reynolds number range, necessitating a comprehensive analysis that considers multiple factors.

Fig. 16 presents the boundary layer velocity profiles at 49% chord length of the Slice 2 section under Reynolds numbers of 5 million and 45 million. At *Re*=5 million, as previously analyzed, the flow at this location is laminar, exhibiting a parabolic velocity distribution. Consequently, roughness has minimal influence in this region. In contrast, at *Re*=45 million, the boundary layer is fully turbulent. With increasing roughness, the boundary layer thickness becomes greater at the same velocity level. This phenomenon explains why the boundary layer thickness increases with roughness.

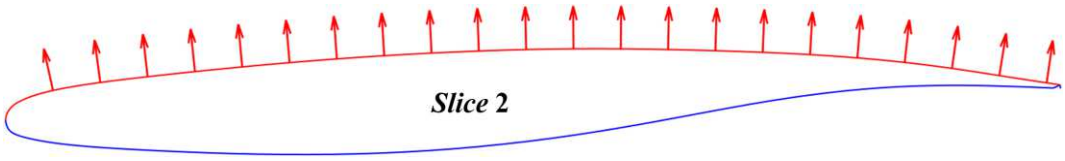
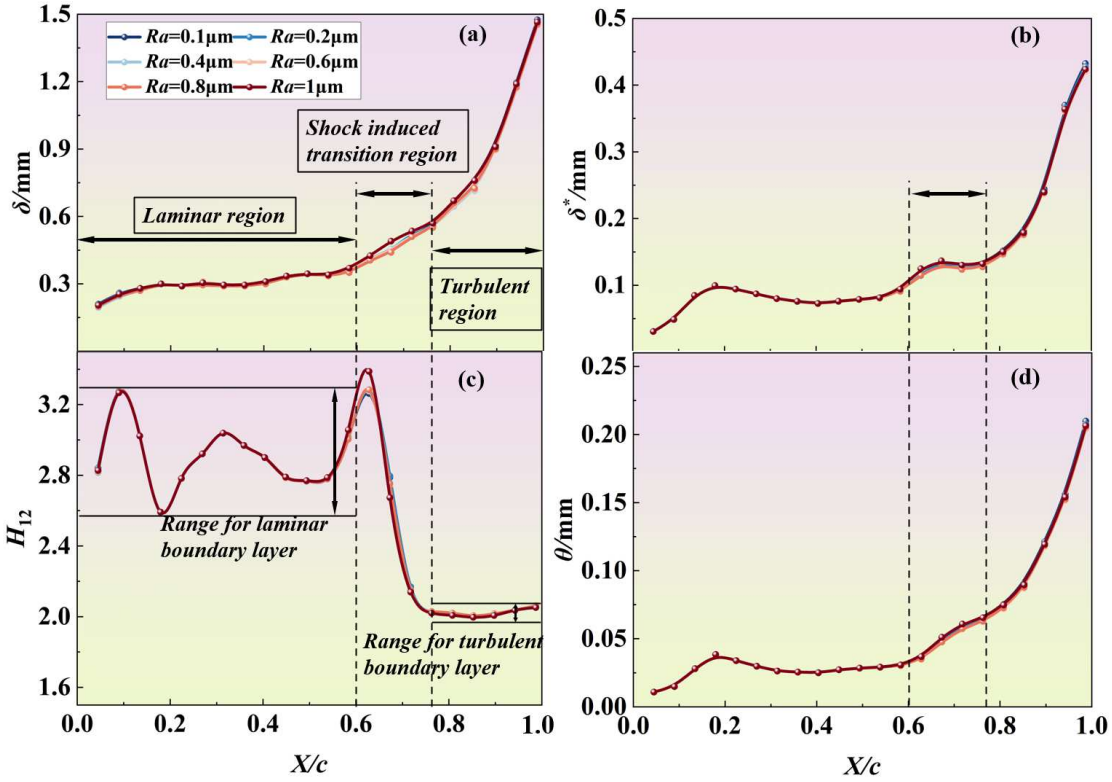
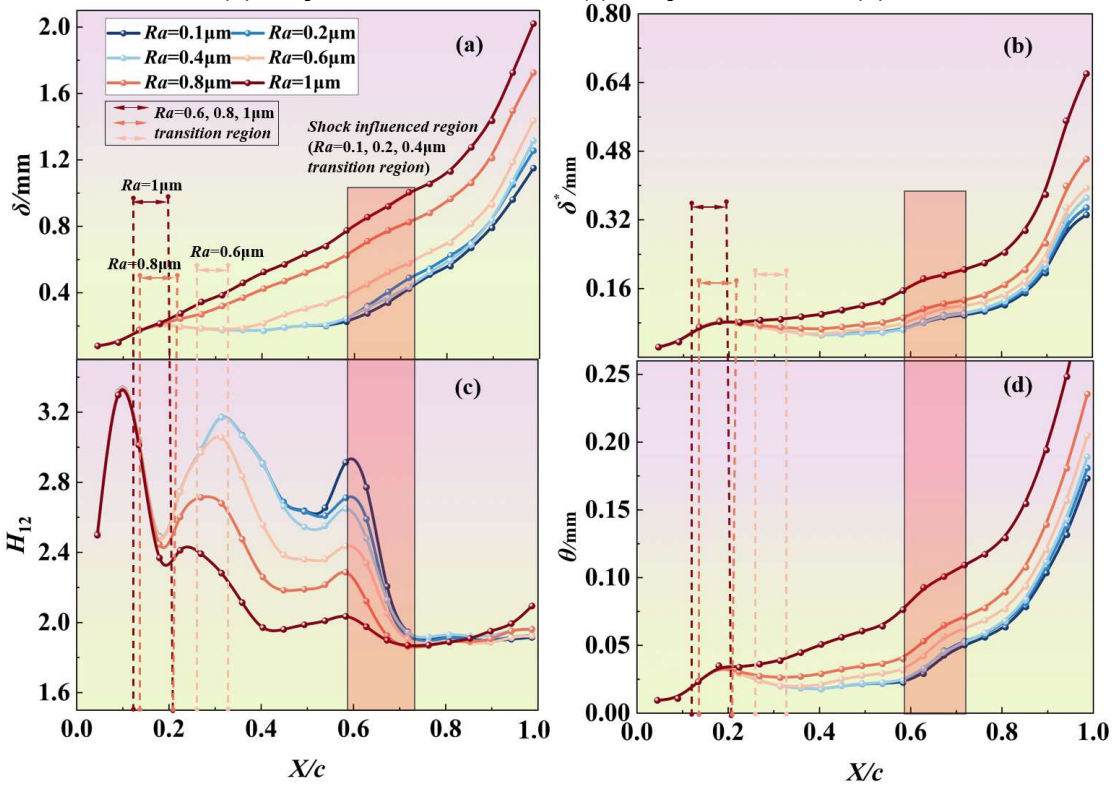


Fig. 11 Schematic of Boundary Layer Extraction at Slice 2



525

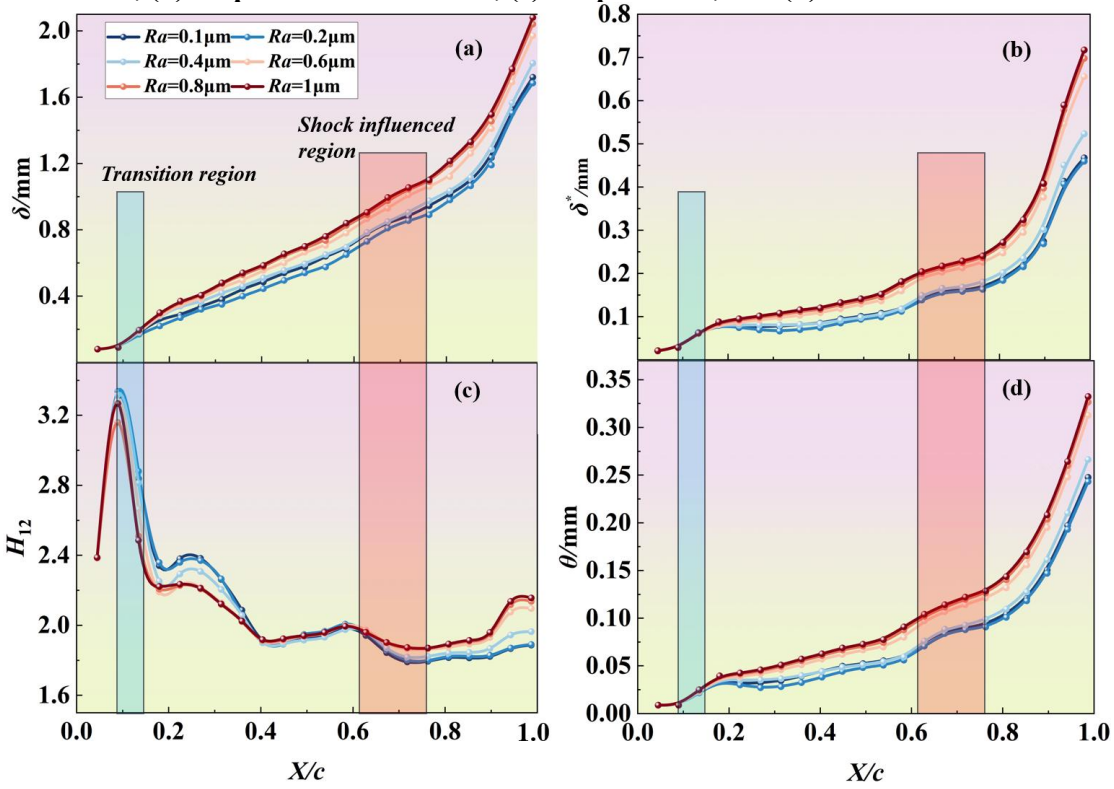
526 **Fig. 12 Boundary Layer Characteristics at Re=5 million, Slice 2: (a) Total Boundary Layer**
527 **Thickness, (b) Displacement Thickness, (c) Shape Factor, and (d) Momentum Thickness**



528

529 **Fig. 13 Boundary Layer Characteristics at Re=10 million, Slice 2: (a) Total Boundary Layer**

530 **Thickness, (b) Displacement Thickness, (c) Shape Factor, and (d) Momentum Thickness**



531

532 **Fig. 14 Boundary Layer Characteristics at Re=15 million, Slice 2: (a) Total Boundary Layer**
533 **Thickness, (b) Displacement Thickness, (c) Shape Factor, and (d) Momentum Thickness**
534

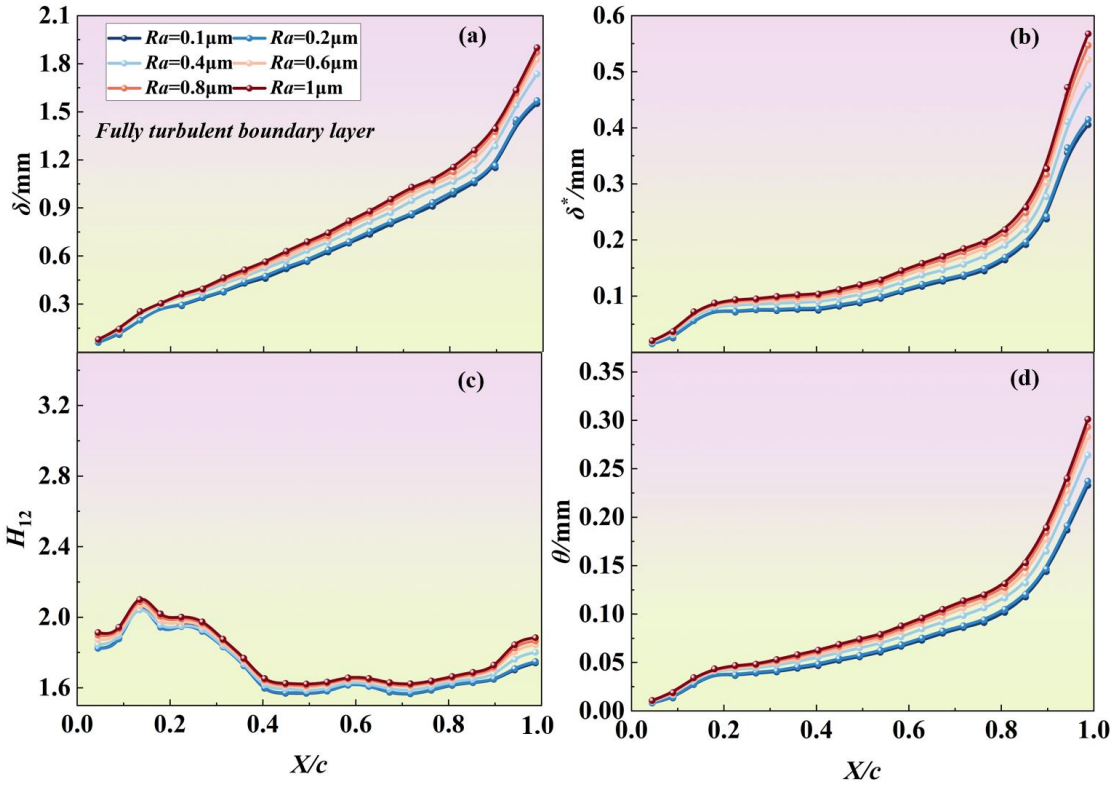
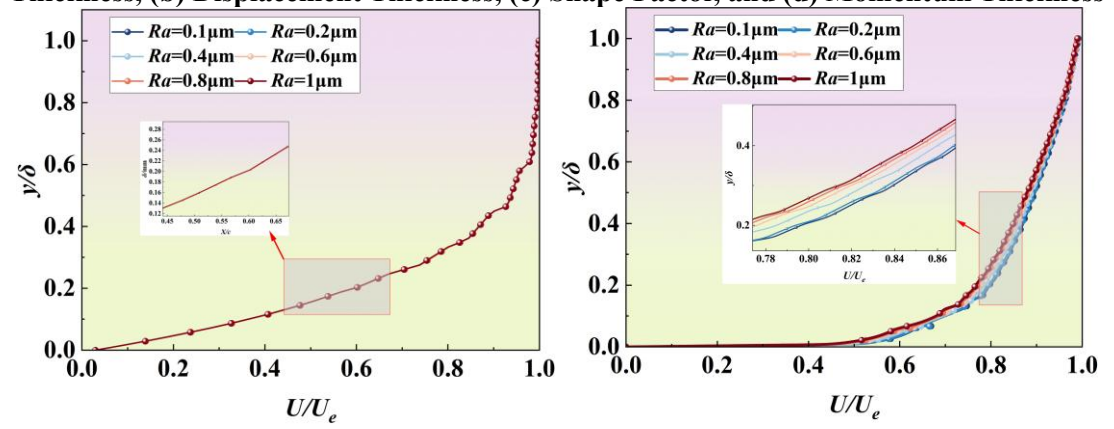


Fig. 15 Boundary Layer Characteristics at Re=45 million, Slice 2: (a) Total Boundary Layer Thickness, (b) Displacement Thickness, (c) Shape Factor, and (d) Momentum Thickness



(a)5million (b)45million

Fig. 16 Boundary Layer Velocity Profiles at Re=5 million and 45 million

Conclusions

This study investigates the aerodynamic performance deviations observed in wind tunnel tests of the wide-body aircraft reference model CHN-T2. Focusing on the discrepancies caused by surface roughness variations, a systematic numerical investigation into the mechanism of micron-level roughness effects

across a wide Reynolds number range was conducted using CFD simulations. The primary conclusions are as follows:

Accumulation of airflow impurities in the wind tunnel environment increases the model surface roughness from 0.1 μm to the 1 μm level. This minor variation significantly impacts the aerodynamic characteristics of transonic aircraft. Numerical simulations indicate that increased roughness causes a distinct upstream shift in the boundary layer transition location, resulting in increased skin friction drag and total drag.

The mechanism of roughness influence demonstrates a strong Reynolds number dependence:At low Reynolds numbers, shock-induced transition dominates; roughness promotes earlier transition by enhancing cross-flow instability.At moderate Reynolds numbers (10–15 million), the influence of roughness intensifies.At high Reynolds numbers, roughness primarily affects the turbulent boundary layer structure, increasing total boundary layer thickness, displacement thickness, and momentum thickness, thereby altering the effective aerodynamic shape.

References

1. Slotnick, J. P. et al. CFD Vision 2030 Study: A Path to Revolutionary Computational Aerosciences. https://ntrs.nasa.gov/citations/20140003093 (2014).

2. Nikuradse, J. Strömungswiderstand in rauhen rohren. Z Angew Math Mech 11, 409–411 (1931).

3. Schlichting, H. Experimentelle untersuchungen zum rauhigkeitsproblem. Ing. Arch 7, 1–34 (1936).

4. Fortin, G., Laforte, J.-L. & Ilinca, A. Heat and mass transfer during ice accretion on aircraft wings with an improved roughness model. International Journal of Thermal Sciences 45, 595–606 (2006).

5. Zheng, C., Jin, Z., Yang, Z. & Yu, L. Effects of scallop ice characteristics on the flow field structures and the aerodynamic performance of an airfoil. Acta Mech 235, 7245–7262 (2024).

6. Uncertainty qualification of aerodynamic performance of a swept wing with ice accretion. Chinese Journal of Aeronautics 38, 103332 (2025).

7. Aerodynamics and ice tolerance of the large passenger aircraft advanced rear end forward swept horizontal tailplane with leading edge extension. Aerospace Science and Technology 161, 110018 (2025).

8. Guan, X., Li, M., Wu, S., Xie, Y. & Sun, Y. Influence of surface ice roughness on the aerodynamic performance of wind turbines. FDMP 20, 2029–2043 (2024).

9. Chen, J., Yang, P., Zhang, Y. & Fu, S. Aerodynamic prediction and roughness implementation toward ice accretion simulation. Physics of Fluids 36, (2024).

10. Ryoo, W.-S., Park, S.-C., Kim, S.-H. & Jeong, J.-H. Elucidation of aerodynamic characteristics due to ice accretion on multi-mw wind turbine blade. J Mech Sci Technol 38, 3989–3995 (2024).

11. Liu, R., Pan, Y., Chen, A., Bin, G. & Li, H. Study on the influence of surface roughness on the erosion characteristics of compressor blades. Powder Technology 430, 119037 (2023).

12. Robin, I., Bennis, A.-C. & Dauvin, J.-C. 3D numerical study of the impact of macro-roughnesses on a tidal turbine, on its performance and hydrodynamic wake. Journal of Marine Science and Engineering 9, 1288 (2021).

13. Performance optimization and investigation of flow phenomena on tidal turbine blade airfoil considering cavitation and roughness. Applied Ocean Research 106, 102463 (2021).

14. Taherkhani, B., Pourkamali Anaraki, A. & Kangarani Farahani, N. Surface roughness effect on turbine blade erosion due to micro-sized particle impact. J Fail. Anal. and Preven. 25, 370–377 (2025).

15. Surface roughness evolution of wind turbine blade subject to rain erosion. Materials & Design 231, 112011 (2023).

16. Control of a boundary layer over a wind turbine blade using distributed passive roughness. Renewable Energy 184, 421–429 (2022).

17. Wu, W., Laguarda, L., Modesti, D. & Hickel, S. Passive control of shock-wave/turbulent boundary-layer interaction using spanwise heterogeneous roughness. Flow Turbulence Combust 115, 29–49 (2025).

18. Aguirre-López, M. A., Hueyotl-Zahuantitla, F., Martínez-Vázquez, P. & Márquez-Urbina, J. U. Passive control of the flow around a rectangular cylinder with a custom rough surface. Fluids 9, 253 (2024).

19. Cheng Hongzhi, Wang Mingyang, Zhou Chuangxin, Zhao Shengfeng, Lu Xingen, Zhu Junqiang, Flow control mechanism of surface roughness of high load axial compressor at low Reynolds number, hkdlxb. 37 (2022) 283–295. https://doi.org/10.13224/j.cnki.jasp.20210134.

20. McKeon, B. J., Jacobi, I. & Duvvuri, S. Dynamic roughness for manipulation and control of turbulent boundary layers: An overview. AIAA Journal 56, 2178–2193 (2018).

21. Huebsch, W. W., Gall, P. D., Hamburg, S. D. & Rothmayer, A. P. Dynamic roughness as a means of leading-edge separation flow control. Journal of Aircraft https://doi.org/10.2514/1.C031350 (2012) doi:10.2514/1.C031350.

22. Cebeci, T. Effects of environmentally imposed roughness on airfoil performance. in (Long Beach, CA, 1987).

606 23. Choudhari, M. M., Li, F., Chang, C.-L. & Edwards, J. On the effects of surface roughness on
607 boundary layer transition. in (Bangalore, 2009).

608 24. Ye, Q., Avallone, F., Ragni, D., Choudhari, M. & Casalino, D. Effect of surface roughness
609 geometry on boundary-layer transition and far-field noise. AIAA Journal 59, 2396–2408 (2021).

610 25. Fan, Y., Zhao, R., Shen, L. & Zhang, X. Improved γ-reθ-ar model for predicting distributed
611 roughness-induced transition. AIAA Journal 63, 2211–2223 (2025).

612 26. Ma, S.-B., Choi, J. & Shim, H.-S. Impact of surface roughness on aerodynamic performance of
613 axial compressor blades under various altitude conditions. Aerospace Science and Technology 164,
614 110368 (2025).

615 27. Dwivedi. Effect of surface roughness on aerodynamic performance of the wing with NACA 4412
616 airfoil at reynolds number 1.7 × 105. Materials Today: Proceedings 56, 468–476 (2022).

617 28. Chakroun, W., Al-Mesri, I. & Al-Fahad, S. Effect of surface roughness on the aerodynamic
618 characteristics of a symmetrical airfoil. Wind Engineering https://doi.org/10.1260/0309524043028136
619 (2004) doi:10.1260/0309524043028136.

620 29. Ehrmann, R., Wilcox, B., White, E. & Maniaci, D. Effect of Surface Roughness on Wind Turbine
621 Performance. SAND--2017-10669, 1596202, 657342 https://www.osti.gov/servlets/purl/1596202/ (2017)
622 doi:10.2172/1596202.

623 30. Lim, S., Ko, Y., Hong, D., Kim, M. & Song, S. J. Impact of additive manufacturing surface
624 roughness on the aerodynamic performance of axial compressor blades. Int. J. Aeronaut. Space Sci. 26,
625 42–49 (2025).

31. Kumar, V., Miró, A., Lehmkuhl, O. & Piomelli, U. Flow separation in airfoils with rough leading edges. AIAA Journal 61, 2035–2047 (2023).

32. Menter, F. R., Langtry, R. & Völker, S. Transition modelling for general purpose CFD codes. Flow Turbulence Combust 77, 277–303 (2006).

33. Knopp, T., Eisfeld, B. & Calvo, J. B. A new extension for *k*–ω turbulence models to account for wall roughness. International Journal of Heat and Fluid Flow 30, 54–65 (2009).

34. RONALD RADEZTSKY, JR., REIBERT, M., SARIC, W. & TAKAGI, S. Effect of micron-sized roughness on transition in swept-wing flows. in 31st Aerospace Sciences Meeting (American Institute of Aeronautics and Astronautics). doi:10.2514/6.1993-76.

35. Crouch, J. D. & Ng, L. L. Variable N-factor method for transition prediction in three-dimensional boundary layers. AIAA Journal 38, 211–216 (2000).

36. Langtry, R. Extending the gamma-rethetat correlation based transition model for crossflow effects (invited). in 45th AIAA Fluid Dynamics Conference (American Institute of Aeronautics and Astronautics, Dallas, TX, 2015). doi:10.2514/6.2015-2474.

37. Griffin, S. A., Madsen, A. P. & Mcclain, A. A. Design Study of Test Models of Maneuvering Aircraft Configurations for the National Transonic Facility (NTF). https://ntrs.nasa.gov/citations/19840025351 (1984).

38. Wang, M. et al. Effects of surface roughness on the aerodynamic performance of a high subsonic compressor airfoil at low reynolds number. Chinese Journal of Aeronautics 34, 71–81 (2021).

Ethics declarations

Competing interests

The authors declare no competing interests.

Tables

Table 1 Geometric and Aerodynamic Parameters of the CHN-T2 Model

Parameter	Value
Fuselage Length/m	63.068
Leading Edge Sweep Angle/°	35.4
Inboard Wing Trailing Edge Sweep/°	0
Outboard Wing Trailing Edge Sweep/°	22
Wingspan/m	61
Aspect Ratio	9.57
Reference Area/m^2	388,65
Reference length/m	8.11
Cruise Mach number	0.85

Table 2 Grid Independence Verification

Mesh	C_L	C_D
Coarse	0.536	0.0252
Midium	0.529	0.0248
Fine	0.525	0.0245

Table 3 Aerodynamic Conditions

Ma	*AOA*	Re_{mac}/million	*TI*
0.85	0°	3.3~45	0.006